JACS
JOURNAL OF THE AMERICAN CHEMICAL SOCIETY
pubs.acs.org/JACS

Fabrication of Functional 3D Nanoarchitectures via Atomic Layer Deposition on DNA Origami Crystals

Arthur Ermatov,[⊥] Melisande Kost,[⊥] Xin Yin, Paul Butler, Mihir Dass, Ian D. Sharp, Tim Liedl, Thomas Bein,* and Gregor Posnjak*

Cite This: J. Am. Chem. Soc. 2025, 147, 9519−9527

Read Online

ACCESS | Metrics & More | Article Recommendations | Supporting Information

ABSTRACT: While DNA origami is a powerful bottom-up fabrication technique, the physical and chemical stability of DNA nanostructures is generally limited to aqueous buffer conditions. Wet chemical silicification can stabilize these structures but does not add further functionality. Here, we demonstrate a versatile three-dimensional (3D) nanofabrication technique to conformally coat micrometer-sized DNA origami crystals with functional metal oxides via atomic layer deposition (ALD). In addition to depositing homogeneous and conformal nanometer-thin ZnO, TiO_2, and IrO_2 (multi)layers inside SiO_2-stabilized crystals, we establish a method to directly coat bare DNA crystals with ALD layers while maintaining the crystal integrity, enabled by critical point drying and low ALD process temperatures. As a proof-of-concept application, we demonstrate electrocatalytic water oxidation using ALD IrO_2-coated DNA origami crystals, resulting in improved performance relative to that of planar films. Overall, our coating strategy establishes a tool set for designing custom-made 3D nanomaterials with precisely defined topologies and material compositions, combining the unique advantages of DNA origami and atomically controlled deposition of functional inorganic materials.

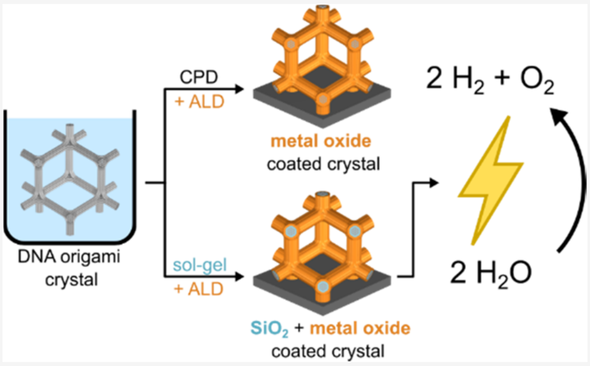

INTRODUCTION

DNA origami[1] is a modular nucleotide-based self-assembly method operating on the molecular level, thereby enabling access to a vast space of advanced nanostructures[2,3] with diverse capabilities, including single molecule placement,[4] reactions[5] and manipulation,[6] chiral plasmonic nanostructures with tailored[7] and switchable[8] optical response, photonic crystals,[9] super-resolution microscopy,[10,11] hierarchically[12] and programmably[13,14] assembled superstructures, drug delivery systems,[15,16] and nanodevices with medical applications.[17,18] DNA nanotechnology thus enables the design of material structure and resulting properties on scales from the single nanometer all the way up to multiple micrometers.[14] The programmable binding of DNA sequences provides both the mechanism for the assembly of the DNA itself as well as the possibility of site-specific decoration of the DNA structures with metallic particles,[7,19] fluorophores,[10,11] proteins,[20,21] and more. In the majority of previously demonstrated applications, DNA origami structures have been used in aqueous buffers since the stability of DNA double helices is highly dependent on pH, salt concentrations, and temperature.[22] To stabilize DNA origami structures, several approaches have been utilized, including covalent bonding,[23] protein coating,[24,25] and silicification using sol−gel chemistry.[26−28] However, the choice of materials that can overgrow DNA by virtue of wet chemistry is limited, and these processes can be difficult to control. Moreover, the materials applied so far have focused on protecting the DNA nanostructure rather than adding further functionality. Coating precisely defined three-dimensional nanostructures with functional materials such as metals,[29] metal oxides, or heterojunctions could yield nanostructures that rival or even outperform three-dimensional (3D) lithographic structures and open a path toward rationally designed 3D meta- and nanomaterials.

While silicification of DNA structures can greatly enhance their mechanical,[28] chemical, and thermal stabilities,[30,31] this wet chemical process is highly dependent on buffer conditions and is prone to poor reproducibility due to inhomogeneous coverage. Furthermore, significant effort is required to optimize the silica thickness and smoothness for the specific nanostructures to be coated. In addition, this approach introduces spatial design constraints due to the thickness of the silica shell, which cannot be controlled as precisely as with

Received: December 3, 2024
Revised: January 27, 2025
Accepted: February 13, 2025
Published: March 6, 2025

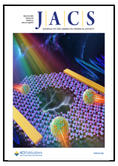

https://doi.org/10.1021/jacs.4c17232

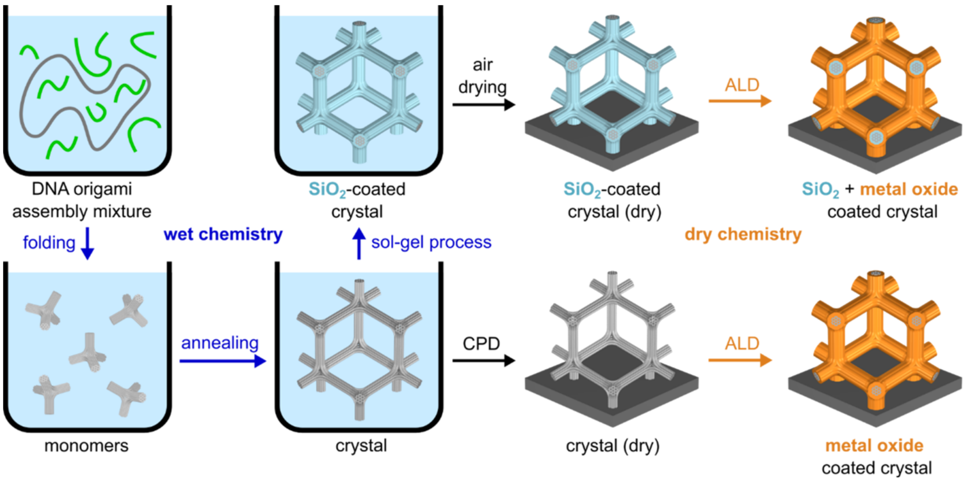

Figure 1. Overview of sample preparation. Folding of DNA origami monomers, crystal annealing, and silica growth are performed in an aqueous 1× Tris-EDTA buffer solution comprising a scaffold strand (gray), staple strands (green), and magnesium ions (not shown). The silicified and bare crystals are then transferred to surfaces (glass or silicon) in liquid and dried in air (following silicification) or via CPD (bare structures without silicification). Finally, various functional metal oxide coatings are grown via ALD.

other coating methods such as atomic layer deposition (ALD). For intricate 3D structures with relatively small pores, it would thus be highly beneficial to circumvent the silicification step and grow a broader range of functional materials with precise thickness control directly onto the DNA; however, capillary forces during drying can deform or collapse intricate nanoscale objects. While recent work[32] reported freeze-drying of individual 3D DNA origami structures, this strategy requires uranyl formate incorporation for stability. An alternative drying method that reduces the deleterious effects of surface tension is critical point drying (CPD),[33] where the solvent is replaced with a liquid that can be brought to the supercritical phase and removed without the liquid−gas phase transition. Even though CPD is widely employed for drying of micro- and nanoscale structures[34,35] and has even been used for extraction of DNA from biological samples,[36] it has not been tested for drying of intricate nanoscale structures that can be assembled with DNA nanotechnology.[37,38] Thus, CPD may offer a route to drying bare DNA origami nanostructures while minimizing structural and morphological deformations.

Atomic layer deposition allows the growth of thin, conformal layers of materials such as metal oxides or pure metals. This is achieved by alternate pulsing of precursor gases, which react in a self-limiting fashion with the chemical groups on the surface of the material. Once the chemical groups have reacted with the first precursor, the reaction has saturated, and the chamber is purged with an inert gas before a second precursor is pulsed into the chamber to form the second part of the deposited layer. These steps are repeated in cycles to grow the coating, thereby enabling precise control of the material thickness down to the number of atomic layers.[39]

Indeed, ALD functionalization of DNA origami structures has been previously shown to be a powerful approach for coating substrate-supported monomeric structures (i.e., flat triangles and triangular prisms) with metal oxides such as aluminum oxide, titanium oxide, and hafnium oxide,[40] as well as platinum.[41] In addition, vapor-phase chemical processes derived from ALD have been demonstrated to be effective in covering silicified 3D DNA nanostructures with metal oxides.[42] However, until now, conventional ALD processes have not been demonstrated to fully penetrate complex 3D DNA origami structures, especially in the absence of SiO_2 stabilization layers.

In this work, we coat micrometer-sized 3D DNA origami crystals with metal oxides using standard ALD processes, showing conformal coating and excellent penetration throughout crystals in sizes up to 10 μm. Not only do we apply this technique to SiO_2-stabilized crystal structures, but we also use a low-temperature ALD process to coat bare DNA origami crystals prepared via a CPD process, thus demonstrating dry chemical stabilization and functionalization of complex 3D DNA nanostructures while preserving their geometry (Figure 1). As a proof-of-concept application of this technique, we demonstrate the functional performance of IrO_2-coated DNA origami crystals deposited on fluorine-doped tin oxide (FTO)/glass supports for the oxygen evolution reaction (OER) via electrocatalytic water oxidation in aqueous environments.

■ RESULTS AND DISCUSSION

ALD Growth on Crystals Stabilized via Sol−Gel Silicification. As the basis for our functional 3D DNA-based nanomaterials, we used DNA origami tetrapods that are designed to assemble into a rod-connected diamond cubic crystal structure.[9] The resulting crystals are 5−10 μm in diameter and possess pore sizes of approximately 100 nm. The cross-section of the connecting rods consists of a 24-helix bundle with a diameter of 15 nm. To grow SiO_2 on the DNA origami with a sol−gel process, we first incubated the crystals in an aqueous buffer with *N*-trimethoxysilyl-propyl-*N*,*N*,*N*-trimethylammonium chloride (TMAPS) before adding tetraethyl orthosilicate (TEOS) and acetic acid[9,26] (experimental details are provided in the Supporting Information (SI)). The silicification process was halted by washing the crystal with water and isopropanol, resulting in a final 24-helix bundle thickness of around 17 nm (Figures S1 and S2). It should be noted that SiO_2 does not only form a thin layer on the surface of the DNA but also infiltrates into the cross-section of the DNA origami,[43] effectively converting the structure into glass. The silicification mechanically stabilizes the DNA origami crystals, allowing air-drying without deformation of the structures.[9,30,44] After the washing steps, the crystals were concentrated and deposited onto silicon or glass surfaces by

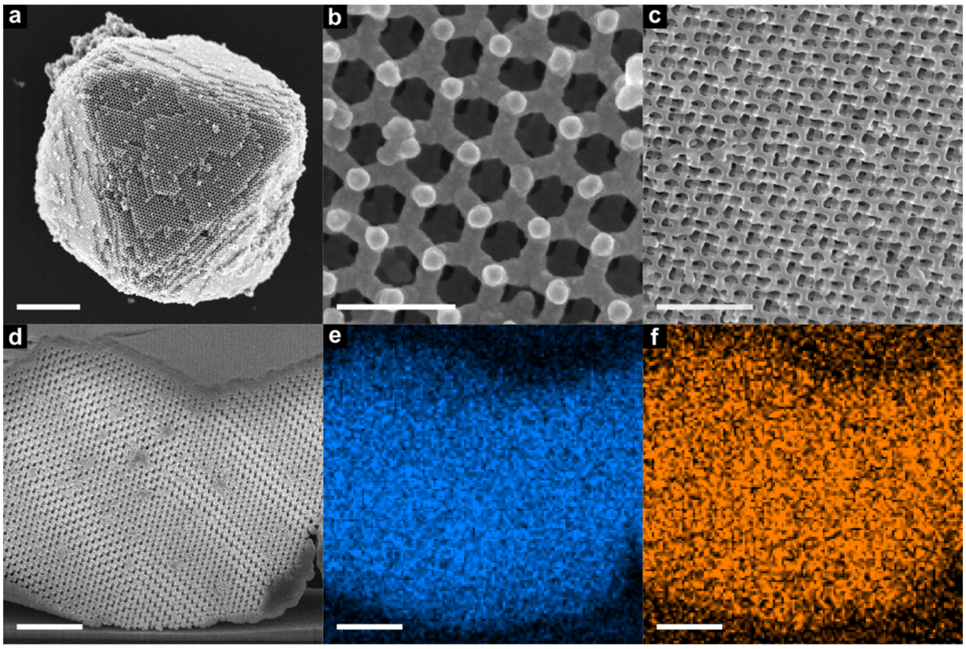

Figure 2. SEM images of DNA origami crystals coated with metal oxides. (a) Top view of an air-dried, silicified crystal after conformal coating with 10 nm of TiO_2 using ALD, scale bar 2 μm. (b) Higher-magnification image of the {111} surface of the crystal shown in panel (a), scale bar 200 nm. (c) Image of the inner region of a crystal obtained by FIB milling of the crystal, scale bar 500 nm. (d–f) Image and composition maps obtained following FIB milling of a silicified crystal coated with two consecutive shells of 5 nm TiO_2 (TTIP process) and 5 nm ZnO; (d) SEM image and corresponding EDX signals for (e) Zn and (f) Ti; all scale bars are 1 μm.

air-drying a droplet of the liquid containing the washed crystals. Subsequently, metal oxides were grown on the dried crystals using ALD. As a proof-of-concept, we used thermal ALD processes based on metal precursors, including diethylzinc (DEZ), tetrakis(dimethylamino)titanium (TDMAT), titanium tetraisopropoxide (TTIP), and iridium acetylacetonate ($Ir(acac)_3$) to grow thin layers of ZnO, TiO_2, and IrO_2 with various thicknesses. Given the thermal stability of SiO_2-stabilized crystals, standard ALD recipes with reactor temperatures in the range of 175–250 °C were used (see the SI for experimental details).

We first analyzed the external surfaces of the ALD-coated crystals with scanning electron microscopy (SEM). In addition, to characterize the interior morphologies of the crystals, we used focused ion beam (FIB) milling to cut open the structures and performed cross-sectional imaging via SEM. The elemental compositions of the inner region of the crystal were subsequently determined by using energy dispersive X-ray spectroscopy (EDX).

Figure 2a–c shows the monocrystalline morphology of the structures after ALD of TiO_2. The crystals primarily grew in octahedral shapes (Figure 2a), with each of the eight triangular surfaces consisting of {111} planes of the diamond cubic lattice and exhibiting a regular hexagonal pattern (Figures 2b and S3).[9] Remarkably, the outer surfaces of the crystals feature very few localized defects. Figure 2c shows the inner structure of the crystal that was exposed by performing an FIB cut perpendicular to the top crystal surface. The plane of the cut was not aligned with any of the crystal planes, resulting in a moiré pattern of interference fringes, where the periodic variation in thickness (Figures 2c and S4) originates from different orientations of the cross-section through the local structure of the lattice.

Importantly, ALD results in conformal growth of the metal oxide throughout the interior of the crystal, as evidenced by the homogeneous distribution of the deposited material observed by EDX mapping. In particular, there is no discernible gradient in the thickness of the coating from the center toward the outer regions, as would be expected in the case of inhomogeneous infiltration of the ALD precursors. Furthermore, we do not observe selective filling or clogging of the lattice pores near the outer surfaces of the monocrystal. While localized aggregation and uneven thicknesses near the external surfaces of the crystal are observed in Figure 2c, their absence in Figure 2a indicates that these imperfections are a consequence of the FIB milling process. Moreover, if clogging of the pores would have occurred during ALD, it would have prevented further penetration into the structure, resulting in thinner coatings inside the crystal, which is not observed.

Many nanotechnological applications require heterostructures comprising several layers of different materials, each serving different purposes (e.g., passivation, charge separation and transport, photon management, chemical or catalytic function, etc.).[45,46] To demonstrate the versatility and robustness of our sample preparation method for the production of mesoscale nanolaminate architectures, we grew heterostructures consisting of two different materials (ZnO and TiO_2, 5 nm thickness each) on top of each other (Figure 2d–f). As for the case of a single ALD layer, we observe a homogeneous pore size (Figure 2d) and elemental distribution (ZnO in Figure 2e and TiO_2 in Figure 2f) across the complete cross-section, indicating that the coverage of such heterostructures is comparable to that of a single material (Figure 2a–c). Thus, this approach of combining both wet chemical and ALD processes enables the creation of mesostructured nanomaterials with smooth and homogeneous layers, in the present case using three different materials (SiO_2, ZnO, and

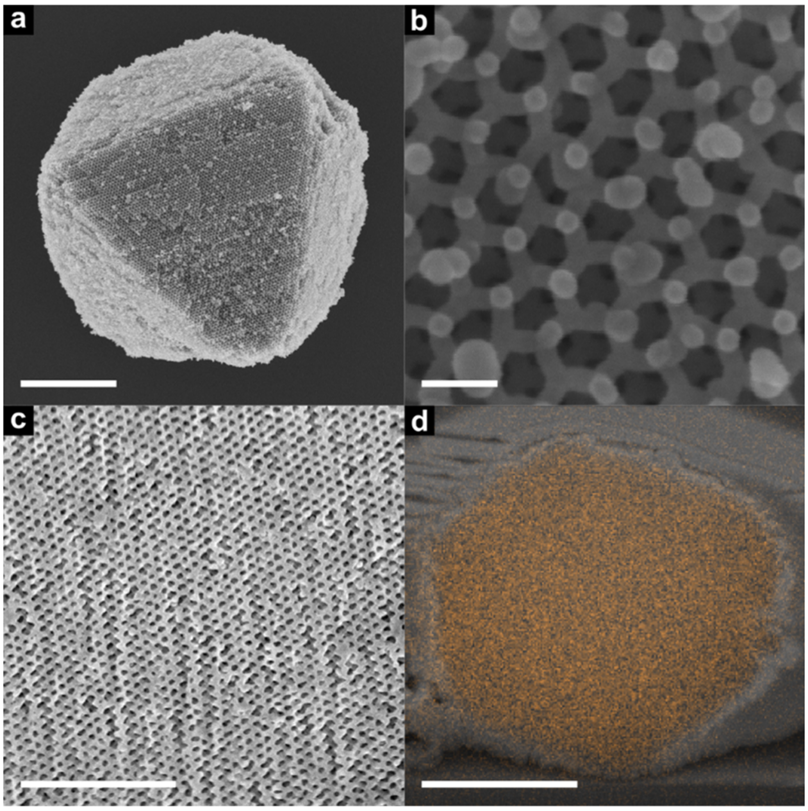

Figure 3. SEM images of CPD-dried crystals. (a) Top view of a DNA origami crystal dried using CPD and subsequently coated with 10 nm of TiO_2 using ALD (TDMAT process, scale bar 2.5 μm). (b) Close-up view of the crystal shown in panel (a) (scale bar 100 nm). (c) Cross-sectional FIB cut of a CPD-dried crystal (scale bar 1 μm). (d) Zoomed-out cross-sectional view of a FIB cut crystal, with the Ti EDX signal overlaid in orange (scale bar 2.5 μm).

TiO_2). While this provides a versatile route to a vast range of complex nanomaterials, we now turn to investigating whether the wet chemical silicification step can be eliminated to grow ALD layers directly on DNA origami crystals.

ALD Growth on Bare DNA Origami Crystals. In order to apply ALD processes on bare crystals, DNA origami structures must first be transferred from the liquid phase to the dry phase. However, air-drying of bare DNA crystals leads to severe morphological deformations and collapse of the intricate crystalline structures (Figures S5 and S6). We attribute this instability to mechanical forces generated by surface tension as the liquid–gas interface moves through the crystal during drying. To overcome this problem, we used CPD based on liquid carbon dioxide (CO_2), which allows transition from the liquid to the gaseous phase via a supercritical fluid phase, thereby avoiding the propagation of a surface tension wave through the sample and associated drying artifacts. In our assembly protocol, bare DNA origami crystals are prepared in an aqueous folding buffer. Since water is poorly soluble in both liquid[47] and supercritical CO_2,[48] the bare crystals were first washed with isopropanol, an intermediate solvent in which both water and CO_2 are soluble. A liquid droplet containing the crystals was then deposited on an ~1 cm^2 rectangle cut from a silicon wafer and placed in an isopropanol bath within the critical point dryer. Next, multiple purging steps were performed, during which liquid CO_2 diluted and replaced the isopropanol. Subsequently, the CO_2 was brought to the supercritical phase and removed (for the complete critical point drying process, see the SI). After CPD drying, the crystals show hardly any deformation (Figure S7).

Once we obtained dried bare DNA origami crystals, we coated them with a 10-nm-thick layer of TiO_2 via ALD using the TDMAT process (see the SI). While the CPD-dried DNA crystals do not show signs of degradation over the course of 6 weeks at room temperature (Figure S8), one of the major obstacles to ALD growth on 3D DNA nanostructures is the potential degradation and deformation of the nanostructure at typical ALD process temperatures.[49] Such instabilities are particularly pronounced if the DNA structures do not have a protective layer, such as SiO_2, that increases their mechanical and thermal stability. Indeed, initial attempts to apply standard 200 °C ALD processes resulted in considerable deformation of bare DNA origami structures (Figure S9). However, by lowering the chamber temperature to 100 °C, we were able to successfully deposit TiO_2 on bare DNA crystals while remaining within the ALD window and preserving their structural integrity (Figure 3).

The crystal morphology was investigated by using SEM imaging of the crystal surface (Figure 3a,b). In contrast to the air-dried bare DNA crystals, which appear deformed and collapsed (Figures S5 and S6), the CPD-dried and TiO_2-coated DNA crystals retain distinct octahedral shapes (Figure 3a) similar to the SiO_2-stabilized crystals (Figure 2a–d). While the top surface of the crystal still displays a hexagonal pattern (Figures 3b and S10), individual hexagons are slightly distorted and less regular than the ones on the surface of the SiO_2-coated crystals in Figure 2a,b. Furthermore, individual tetrahedron arms appear to be slightly bent. These distortions can be attributed to drying artifacts due to the reduced rigidity of the bare DNA structure compared to the silicified crystals.

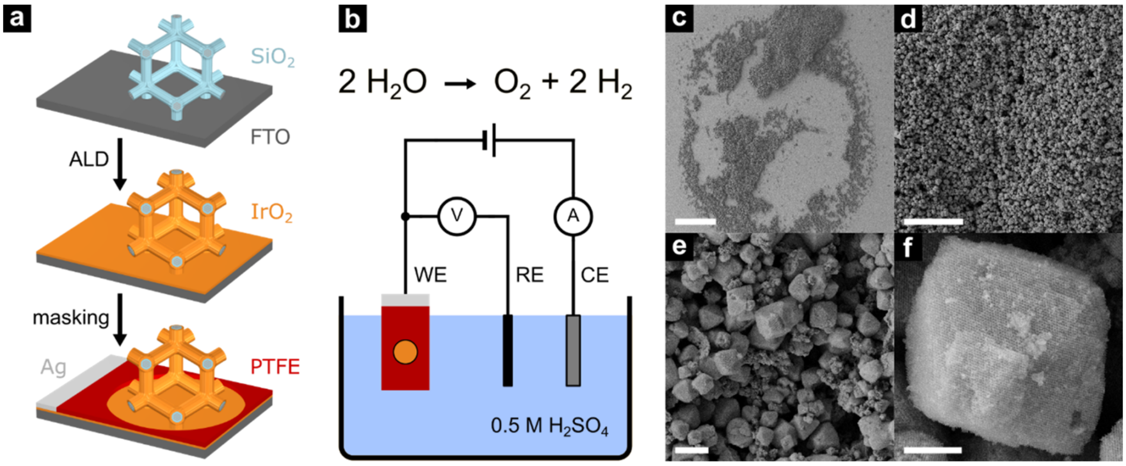

Figure 4. Experimental setup for electrocatalytic water oxidation using functionalized DNA origami crystals. (a) Sample preparation: Silicified DNA origami crystals were deposited and air-dried on an FTO-coated glass substrate. A thin layer of IrO_2 was subsequently grown via ALD, resulting in conformal deposition on both the exposed FTO substrate and on the SiO_2-coated DNA crystals. The substrate was then masked with PTFE, leaving an exposed 5 mm diameter circular area containing all of the DNA crystals. A separate exposed region on the edge of the sample was also defined, on which a Ag contact was placed. (b) Experimental three-electrode setup for electrocatalytic water oxidation with IrO_2-coated DNA origami crystals. (c−f) Exemplary SEM images of a 3× concentrated DNA origami crystal sample supported on FTO and coated with IrO_2 via ALD at different magnifications ((c) scale bar 500 μm, (d) scale bar 100 μm, (e) scale bar 10 μm, and (f) scale bar 2 μm).

Nevertheless, long-range ordering is retained and future optimization of drying protocols may be applied to minimize these comparatively minor structural distortions.

Analogous to the SiO_2-stabilized crystals, the ALD-coated bare crystals were cut using FIB milling, and both their structure and material composition were analyzed using SEM and EDX, respectively. Remarkably, the overall crystal morphology (Figure 3c) is preserved during the drying and ALD processes. However, regular moiré patterns that were obtained for SiO_2-stabilized crystals (Figure 2c−d) are not observed. We attribute this lack of interference between the cut surface and the crystal planes to the slight distortion of the crystal, resulting from the drying process. Nevertheless, the quality of the deposition of TiO_2 on the bare DNA crystals is comparable to that obtained with the ALD process on SiO_2-stabilized crystals (Figure 3d). Similar to the ALD of two different materials shown for SiO_2-coated crystals in Figure 2, we expect this process to work equally for several layers of different materials as long as the first material is deposited at chamber temperatures that do not compromise the mechanical stability of the DNA crystal.

IrO_2-Facilitated Electrocatalytic Water Splitting. Among many other applications, the ALD-covered DNA origami crystals are potentially interesting for electrochemical,[50] photoelectrochemical, and photochemical[51] energy conversion due to the large surface-to-volume ratios associated with their porous structures. Furthermore, these crystals could form hierarchical porous systems with diverse topologies and a vast range of scaffold structures, compositions, and surface functionalities, all of which can be tuned to, for example, beneficially promote light absorption, charge carrier transport, mass transport, and catalytic activity. Here, we illustrate these opportunities with a proof-of-concept OER catalyst for electrochemical water splitting based on IrO_2-coated DNA origami crystals. Key questions that can be systematically addressed and ultimately optimized with DNA origami crystals include the electrical contact with a conducting electrode surface, electrical conductivity through the coated origami structure (depending on bulk oxide and Ir-oxide conductivity), catalytic surface area, mechanical stability of crystal attachment, chemical stability of the Ir-oxide phase, and oxygen gas evolution management. The latter will be strongly dependent on the current density, pore structure, and layer thickness or crystal size. While a systematic study of these important aspects is beyond the scope of this work and will be the subject of future research, here we show that the Ir-oxide-coated DNA crystals indeed feature significant electrocatalytic OER activity.

To generate electrochemically active anodes, we coated the DNA origami crystals with an ∼3-nm-thick layer of IrO_2 and used them as a catalyst for the OER[52] (Figure 4). Using DNA origami monomers as the basis for the crystal, geometry and pore sizes can be precisely controlled. In this proof-of-concept demonstration, our crystals possess a pore diameter of approximately 100 nm and exhibit a surface-to-volume ratio of $1.88 \times 10^7\ \mathrm{m}^{-1}$ (see the SI for calculation). These dimensions place our system in an intermediate regime compared to previous OER studies that have investigated the impact of pore sizes, either in the range of a few nanometers[53] or up to micrometers[54] in diameter.

Silicified crystals were deposited on glass substrates coated with FTO (Figure 4a,c−f). Since silicified DNA crystals can be air-dried, a solution containing the crystals can be applied to substrates and air-dried several times in a row, allowing for a degree of control over surface coverage and sample thickness. To determine the impact of surface loading, we examined two different coverages denoted as "1× DNA" and "3× DNA", where "1× DNA" comprises one deposition cycle with an estimated 0.28 pmol of crystal monomers, resulting in a total IrO_2-covered surface of approximately 20 cm^2, with the corresponding values for "3× DNA" being 3-fold higher (note that these values are estimates based on the origami geometry, see the SI for assumptions and calculation). FTO-coated glass slides without any deposited crystals were used as nominally planar reference samples. After drying, samples were coated with IrO_2 via ALD and subsequently placed in a three-electrode electrochemical cell containing sulfuric acid (Figure 4b). Cyclic voltammetry was performed with the IrO_2-coated samples configured as the working electrode and with a fixed

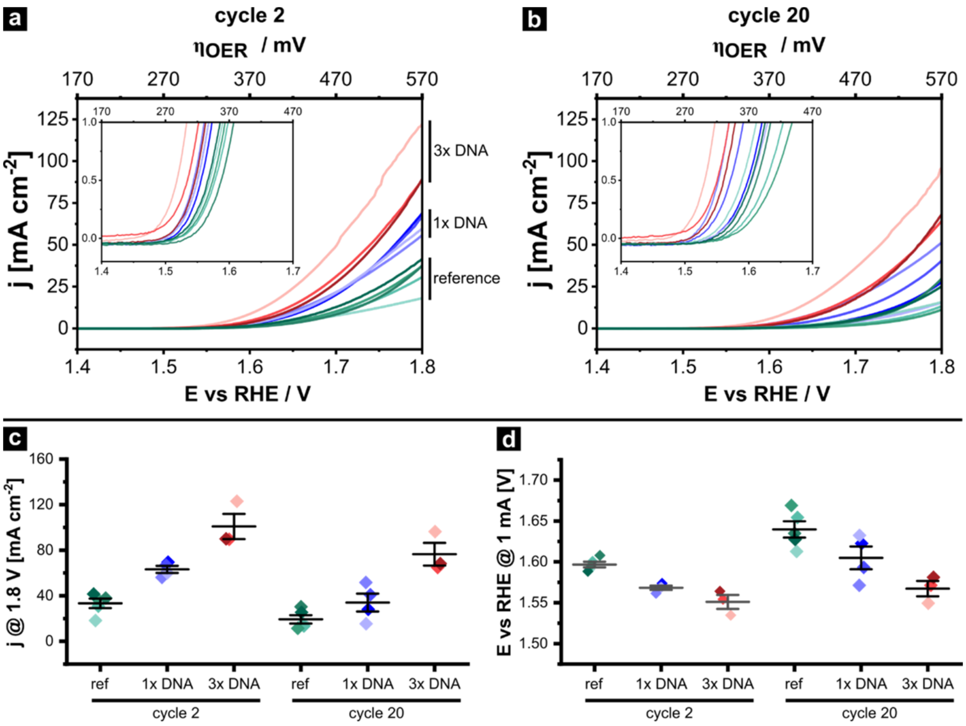

Figure 5. Electrolysis of water with IrO_2-coated DNA origami crystals. The specific color shade of each curve and point represents an individual sample. The reference ("ref") data (green shades) refer to FTO-covered glass substrates with 5.1 nm of IrO_2, without any DNA origami crystals. "1× DNA" (blue shades) denotes 0.28 pmol of crystal monomers deposited on the FTO-glass surface, and ″3× DNA" (red shades) denotes samples produced with three times as much material, as described in the text. (a, b) Current density as a function of applied electrochemical potential measured in (a) cycle 2 and (b) cycle 20. Insets show zoomed-in regions near the onset potential. (c) Statistical analysis of current density at 1.8 V vs RHE. (d) Statistical analysis of the electrochemical potential required to reach a current density of 1 mA/cm^2.

scan rate of 20 mV/s (Figure 5a,b). While the first cycle was performed from 0 V vs reversible hydrogen electrode (RHE) to 1.8 V vs RHE, all subsequent cycles were run from 1.0 V vs RHE to 1.8 V vs RHE, for a total of 20 cycles. In the following, we discuss the key performance metrics obtained from these proof-of-concept DNA-origami-based electrocatalysts, as well as future opportunities and needs for rational design and improvement of such catalytic systems.

An approximately linear enhancement in catalytic activity with increasing crystal concentration is observed and is compared with the reference samples (Figure 5c). However, the enhancement is not proportional to the increase in the surface area of the sample; although the "1× DNA" samples had an approximately 100× larger surface area than the reference sample, the catalytic activity is enhanced only by a factor of 1.9 (during cycle 2). For the "3× DNA" samples, the enhancement factor during cycle 2 was approximately 3 (for cycle 20: corresponding enhancement factors were 1.8 for "1× DNA", 4 for "3× DNA"). Nevertheless, we observe a decrease in the onset potential at 1 mA/cm^2 (Figure 5d) with increasing density of crystals, reflecting the increase in the overall electrocatalytic activity. The narrow scatter range of the samples in Figure 5d suggests consistent IrO_2 coverage over the catalytically active surface.

The moderate current density increases suggest that only a fraction of IrO_2 contributes to the overall activity, which likely originates from two factors that should be addressed in future work. First, while IrO_2 thin films possess high electrical conductivities[55] and the IrO_2 coverage inside individual crystals is homogeneous (Figure S11), the contact between the crystals, and between the crystals and the substrate, may limit electrical transport to and from catalytically active sites. To overcome this limitation, possible future strategies could include the integration of additional conducting layers prior to IrO_2 coating or directed growth of oriented DNA crystal films on (prefunctionalized) substrates. Second, it is likely that the nanoscale mass transport is limited within the crystals. For example, the oxygen that is produced during the catalytic reaction can be entrapped within the relatively small pores of the crystals and can reduce the contact area of water with the catalyst. This would reduce the catalytically active area and hence limit the reaction rate within the crystal. Previous work suggested that efficient detachment, transport, and coalescence of gas bubbles is also modulated by the 3D geometry of the catalyst, demonstrated by the differences in catalytic activity for pore sizes ranging from 200 to 1200 nm.[54] This hypothesis can be tested in future experiments by using DNA crystal designs with varying unit cell dimensions and topologies optimized for mass transfer, enabled by the versatile topological and geometric design of DNA crystals.

We further observed a decrease in the catalytic activity after 20 CV cycles. We hypothesize that this is due to two reasons. First, IrO_2 is known to slowly dissolve under OER conditions,[56,57] which is also observed in the present work and manifests for the reference samples as a decrease of the current density and increase of the overpotential between cycle 2 and cycle 20, as shown in Figure 5. Second, crystals can detach from the surface (Figure S12, blue box) due to mechanical stresses generated during bubble formation and evolution. Here, we note that the crystals are only physically deposited on the surface and adhere due to a combination of weak van der Waals forces and the thin metal oxide layer deposited via ALD, making them prone to mechanical detachment from the sample surface. This is further exacerbated by the "open" configuration of the working electrode electrochemical half-cell, which allows detached crystals to disperse into the bulk electrolyte. By comparison, such effects can likely be suppressed in more confined designs, such as membrane electrode assemblies or through the use of ionomer binders. Interestingly, the crystals not only appear to detach but also to partially reattach to the IrO_2 surface at different locations (Figure S12, red boxes), highlighting the dynamic nature of the working interface. Nevertheless, the morphology of the crystals themselves is not altered during the electrochemical experiment (Figure S13), indicating significant structural stability under harsh acidic conditions and demonstrating the robustness of the SiO_2- and ALD-coated crystals.

■ CONCLUSIONS

We demonstrated the fabrication of 3D nanomaterials with controlled pore topologies and dimensions by coating micrometer-sized SiO_2-coated DNA origami crystals with metal oxides such as ZnO, TiO_2, and IrO_2. The porous 3D materials were conformally coated by ALD, with homogeneous layers extending through the complete internal volume of these intricate nanostructures. Furthermore, we demonstrated a method to transfer bare DNA crystals from the liquid to the dry phase while preserving their structures, allowing us to use ALD to grow TiO_2 directly on DNA. As an example application of the developed methods, we show a proof-of-principle study of IrO_2-based electrocatalytic water splitting, demonstrating enhanced catalytic performance compared with planar surfaces. The techniques demonstrated here greatly expand the range of potential applications based on DNA origami-based nano- and mesostructures, providing unique possibilities in terms of the versatile design, precise molecular arrangement, and ALD-based functionalization.

■ ASSOCIATED CONTENT

Supporting Information

The Supporting Information is available free of charge at https://pubs.acs.org/doi/10.1021/jacs.4c17232.

Additional experimental details, materials and methods; and additional experimental figures (PDF)

■ AUTHOR INFORMATION

Corresponding Authors

Thomas Bein − *Department of Chemistry and CeNS, Ludwig-Maximilians-Universität München, 81377 München, Germany*; orcid.org/0000-0001-7248-5906; Email: bein@lmu.de

Gregor Posnjak − *Faculty of Physics and CeNS, Ludwig-Maximilians-Universität München, 80539 München, Germany*; orcid.org/0000-0002-9863-4444; Email: gregor.posnjak@physik.lmu.de

Authors

Arthur Ermatov − *Faculty of Physics and CeNS, Ludwig-Maximilians-Universität München, 80539 München, Germany*; orcid.org/0009-0004-2356-7381

Melisande Kost − *Department of Chemistry and CeNS, Ludwig-Maximilians-Universität München, 81377 München, Germany*

Xin Yin − *Faculty of Physics and CeNS, Ludwig-Maximilians-Universität München, 80539 München, Germany*

Paul Butler − *Walter Schottky Institute, Technical University of Munich, 85748 München, Germany; Physics Department, TUM School of Natural Sciences, Technical University of Munich, 85748 München, Germany*

Mihir Dass − *Faculty of Physics and CeNS, Ludwig-Maximilians-Universität München, 80539 München, Germany*

Ian D. Sharp − *Walter Schottky Institute, Technical University of Munich, 85748 München, Germany; Physics Department, TUM School of Natural Sciences, Technical University of Munich, 85748 München, Germany*; orcid.org/0000-0001-5238-7487

Tim Liedl − *Faculty of Physics and CeNS, Ludwig-Maximilians-Universität München, 80539 München, Germany*; orcid.org/0000-0002-0040-0173

Complete contact information is available at: https://pubs.acs.org/10.1021/jacs.4c17232

Author Contributions

$^{\perp}$A.E. and M.K. contributed equally to this project..

Notes

The authors declare no competing financial interest.

■ ACKNOWLEDGMENTS

The authors thank Dr. Steffen Schmidt for his help with the FIB lithography and the corresponding SEM and EDX images. M.K. expresses her gratitude to Robert von Kalle for the reliable and secure transportation of the samples between the various locations. A.E., X.Y., M.D., T.L., and G.P. acknowledge funding from the ERC consolidator grant "DNA Funs" (Project ID 818635), the Federal Ministry of Education and Research (BMBF), and the Free State of Bavaria under the Excellence Strategy of the Federal Government and the Länder through the ONE MUNICH Projects Munich Multiscale Biofabrication and Enabling Quantum Communication and Imaging Applications. T.B. acknowledges funding from the German Federal Ministry of Education and Research (BMBF) within the Kopernikus Project P2X: Flexible use of renewable resources—research, validation, and implementation of "Power-to-X" concepts (Project Numbers 3SFK2P0-2 and 3SFK2Z0-2) as well as Project 03HY129C IRIDIOS and from the Bavarian research network "Solar Technologies Go Hybrid". The authors thank the e-conversion Cluster of Excellence (Deutsche Forschungsgemeinschaft (DFG, German Research Foundation) EXC 2089/1-390776260) for financial support.

■ REFERENCES

(1) Rothemund, P. W. K. Folding DNA to Create Nanoscale Shapes and Patterns. *Nature* **2006**, *440* (7082), 297−302.

(2) Douglas, S. M.; Dietz, H.; Liedl, T.; Högberg, B.; Graf, F.; Shih, W. M. Self-Assembly of DNA into Nanoscale Three-Dimensional Shapes. *Nature* **2009**, *459* (7245), 414−418.

(3) Douglas, S. M.; Marblestone, A. H.; Teerapittayanon, S.; Vazquez, A.; Church, G. M.; Shih, W. M. Rapid Prototyping of 3D DNA-Origami Shapes with CaDNAno. *Nucleic Acids Res.* **2009**, *37* (15), 5001−5006.

(4) Gopinath, A.; Thachuk, C.; Mitskovets, A.; Atwater, H. A.; Kirkpatrick, D.; Rothemund, P. W. K. Absolute and Arbitrary Orientation of Single-Molecule Shapes. *Science* **2021**, *371* (6531), No. eabd6179.

(5) Voigt, N. V.; Tørring, T.; Rotaru, A.; Jacobsen, M. F.; Ravnsbæk, J. B.; Subramani, R.; Mamdouh, W.; Kjems, J.; Mokhir, A.; Besenbacher, F.; Gothelf, K. V. Single-Molecule Chemical Reactions on DNA Origami. *Nat. Nanotechnol.* **2010**, *5* (3), 200−203.

(6) Nickels, P. C.; Wünsch, B.; Holzmeister, P.; Bae, W.; Kneer, L. M.; Grohmann, D.; Tinnefeld, P.; Liedl, T. Molecular Force Spectroscopy with a DNA Origami−Based Nanoscopic Force Clamp. *Science* **2016**, *354* (6310), 305−307.

(7) Kuzyk, A.; Schreiber, R.; Fan, Z.; Pardatscher, G.; Roller, E.-M.; Högele, A.; Simmel, F. C.; Govorov, A. O.; Liedl, T. DNA-Based Self-Assembly of Chiral Plasmonic Nanostructures with Tailored Optical Response. *Nature* **2012**, *483* (7389), 311−314.

(8) Kuzyk, A.; Schreiber, R.; Zhang, H.; Govorov, A. O.; Liedl, T.; Liu, N. Reconfigurable 3D Plasmonic Metamolecules. *Nat. Mater.* **2014**, *13* (9), 862−866.

(9) Posnjak, G.; Yin, X.; Butler, P.; Bienek, O.; Dass, M.; Lee, S.; Sharp, I. D.; Liedl, T. Diamond-Lattice Photonic Crystals Assembled from DNA Origami. *Science* **2024**, *384* (6697), 781−785.

(10) Reinhardt, S. C. M.; Masullo, L. A.; Baudrexel, I.; Steen, P. R.; Kowalewski, R.; Eklund, A. S.; Strauss, S.; Unterauer, E. M.; Schlichthaerle, T.; Strauss, M. T.; Klein, C.; Jungmann, R. Ångström-Resolution Fluorescence Microscopy. *Nature* **2023**, *617* (7962), 711−716.

(11) Jungmann, R.; Avendaño, M. S.; Woehrstein, J. B.; Dai, M.; Shih, W. M.; Yin, P. Multiplexed 3D Cellular Super-Resolution Imaging with DNA-PAINT and Exchange-PAINT. *Nat. Methods* **2014**, *11* (3), 313−318.

(12) Wagenbauer, K. F.; Sigl, C.; Dietz, H. Gigadalton-Scale Shape-Programmable DNA Assemblies. *Nature* **2017**, *552* (7683), 78−83.

(13) Tikhomirov, G.; Petersen, P.; Qian, L. Fractal Assembly of Micrometre-Scale DNA Origami Arrays with Arbitrary Patterns. *Nature* **2017**, *552* (7683), 67−71.

(14) Wintersinger, C. M.; Minev, D.; Ershova, A.; Sasaki, H. M.; Gowri, G.; Berengut, J. F.; Corea-Dilbert, F. E.; Yin, P.; Shih, W. M. Multi-Micron Crisscross Structures Grown from DNA-Origami Slats. *Nat. Nanotechnol.* **2023**, *18* (3), 281−289.

(15) Zhao, Y.-X.; Shaw, A.; Zeng, X.; Benson, E.; Nyström, A. M.; Högberg, B. DNA Origami Delivery System for Cancer Therapy with Tunable Release Properties. *ACS Nano* **2012**, *6* (10), 8684−8691.

(16) Andersen, E. S.; Dong, M.; Nielsen, M. M.; Jahn, K.; Subramani, R.; Mamdouh, W.; Golas, M. M.; Sander, B.; Stark, H.; Oliveira, C. L. P.; Pedersen, J. S.; Birkedal, V.; Besenbacher, F.; Gothelf, K. V.; Kjems, J. Self-Assembly of a Nanoscale DNA Box with a Controllable Lid. *Nature* **2009**, *459* (7243), 73−76.

(17) Jiang, D.; Ge, Z.; Im, H.-J.; England, C. G.; Ni, D.; Hou, J.; Zhang, L.; Kutyreff, C. J.; Yan, Y.; Liu, Y.; et al. DNA Origami Nanostructures Can Exhibit Preferential Renal Uptake and Alleviate Acute Kidney Injury. *Nat. Biomed. Eng.* **2018**, *2* (11), 865−877.

(18) Sigl, C.; Willner, E. M.; Engelen, W.; Kretzmann, J. A.; Sachenbacher, K.; Liedl, A.; Kolbe, F.; Wilsch, F.; Aghvami, S. A.; Protzer, U.; Hagan, M. F.; Fraden, S.; Dietz, H. Programmable Icosahedral Shell System for Virus Trapping. *Nat. Mater.* **2021**, *20* (9), 1281−1289.

(19) Liu, W.; Tagawa, M.; Xin, H. L.; Wang, T.; Emamy, H.; Li, H.; Yager, K. G.; Starr, F. W.; Tkachenko, A. V.; Gang, O. Diamond Family of Nanoparticle Superlattices. *Science* **2016**, *351* (6273), 582−586.

(20) Huang, J.; Jaekel, A.; van den Boom, J.; Podlesainski, D.; Elnaggar, M.; Heuer-Jungemann, A.; Kaiser, M.; Meyer, H.; Saccà, B. A Modular DNA Origami Nanocompartment for Engineering a Cell-Free, Protein Unfolding and Degradation Pathway. *Nat. Nanotechnol.* **2024**, *19* (10), 1521−1531.

(21) Xiong, Y.; Huang, J.; Wang, S.-T.; Zafar, S.; Gang, O. Local Environment Affects the Activity of Enzymes on a 3D Molecular Scaffold. *ACS Nano* **2020**, *14* (11), 14646−14654.

(22) Ramakrishnan, S.; Ijäs, H.; Linko, V.; Keller, A. Structural Stability of DNA Origami Nanostructures under Application-Specific Conditions. *Comput. Struct. Biotechnol. J.* **2018**, *16*, 342−349.

(23) Gerling, T.; Kube, M.; Kick, B.; Dietz, H. Sequence-Programmable Covalent Bonding of Designed DNA Assemblies. *Sci. Adv.* **2018**, *4* (8), No. eaau1157.

(24) Auvinen, H.; Zhang, H.; Nonappa; Kopilow, A.; Niemelä, E. H.; Nummelin, S.; Correia, A.; Santos, H. A.; Linko, V.; Kostiainen, M. A. Protein Coating of DNA Nanostructures for Enhanced Stability and Immunocompatibility. *Adv. Healthcare Mater.* **2017**, *6* (18), No. 1700692.

(25) Ponnuswamy, N.; Bastings, M. M. C.; Nathwani, B.; Ryu, J. H.; Chou, L. Y. T.; Vinther, M.; Li, W. A.; Anastassacos, F. M.; Mooney, D. J.; Shih, W. M. Oligolysine-Based Coating Protects DNA Nanostructures from Low-Salt Denaturation and Nuclease Degradation. *Nat. Commun.* **2017**, *8* (1), No. 15654.

(26) Nguyen, L.; Döblinger, M.; Liedl, T.; Heuer-Jungemann, A. DNA-Origami-Templated Silica Growth by Sol−Gel Chemistry. *Angew. Chem., Int. Ed.* **2019**, *58* (3), 912−916.

(27) Liu, X.; Zhang, F.; Jing, X.; Pan, M.; Liu, P.; Li, W.; Zhu, B.; Li, J.; Chen, H.; Wang, L.; Lin, J.; Liu, Y.; Zhao, D.; Yan, H.; Fan, C. Complex Silica Composite Nanomaterials Templated with DNA Origami. *Nature* **2018**, *559* (7715), 593−598.

(28) Michelson, A.; Flanagan, T. J.; Lee, S.-W.; Gang, O. High-Strength, Lightweight Nano-Architected Silica. *Cell Rep. Phys. Sci.* **2023**, *4* (7), No. 101475.

(29) Shani, L.; Michelson, A. N.; Minevich, B.; Fleger, Y.; Stern, M.; Shaulov, A.; Yeshurun, Y.; Gang, O. DNA-Assembled Superconducting 3D Nanoscale Architectures. *Nat. Commun.* **2020**, *11* (1), No. 5697.

(30) Majewski, P. W.; Michelson, A.; Cordeiro, M. A. L.; Tian, C.; Ma, C.; Kisslinger, K.; Tian, Y.; Liu, W.; Stach, E. A.; Yager, K. G.; Gang, O. Resilient Three-Dimensional Ordered Architectures Assembled from Nanoparticles by DNA. *Sci. Adv.* **2021**, *7* (12), No. eabf0617.

(31) Martynenko, I. V.; Erber, E.; Ruider, V.; Dass, M.; Posnjak, G.; Yin, X.; Altpeter, P.; Liedl, T. Site-Directed Placement of Three-Dimensional DNA Origami. *Nat. Nanotechnol.* **2023**, *18*, 1456−1462.

(32) Zhou, F.; Sun, W.; Zhang, C.; Shen, J.; Yin, P.; Liu, H. 3D Freestanding DNA Nanostructure Hybrid as a Low-Density High-Strength Material. *ACS Nano* **2020**, *14* (6), 6582−6588.

(33) Anderson, T. F. Techniques for the Preservaation of Three-Dimensional Structure in Preparing Specimens for the Electron Microscope. *Trans. N. Y. Acad. Sci.* **1951**, *13* (4), 130−134.

(34) van Bommel, M. J.; de Haan, A. B. Drying of Silica Aerogel with Supercritical Carbon Dioxide. *J. Non-Cryst. Solids* **1995**, *186*, 78−82.

(35) Jafri, I. H.; Busta, H.; Walsh, S. T. In *Critical Point Drying and Cleaning for MEMS Technology*, SPIE Proceedings; SPIE, 1999; pp 51−58.

(36) Dillon, N.; Austin, A. D.; Bartowsky, E. Comparison of Preservation Techniques for DNA Extraction from Hymenopterous Insects. *Insect Mol. Biol.* **1996**, *5* (1), 21−24.

(37) Li, X.; Wang, J.; Baptist, A.; Wu, W.; Heuer-Jungemann, A.; Zhang, T. Crystalline Assemblies of DNA Nanostructures and Their Functional Properties. *Angew. Chem., Int. Ed.* **2025**, *64* (3), No. e202416948.

(38) Lee, J.; Kim, J.; Posnjak, G.; Ershova, A.; Hayakawa, D.; Shih, W. M.; Rogers, W. B.; Ke, Y.; Liedl, T.; Lee, S. DNA Origami Colloidal Crystals: Opportunities and Challenges. *Nano Lett.* **2025**, *25* (1), 16−27.

(39) Leskelä, M.; Ritala, M. Atomic Layer Deposition (ALD): From Precursors to Thin Film Structures. *Thin Solid Films* **2002**, *409* (1), 138−146.

(40) Hui, L.; Nixon, R.; Tolman, N.; Mukai, J.; Bai, R.; Wang, R.; Liu, H. Area-Selective Atomic Layer Deposition of Metal Oxides on DNA Nanostructures and Its Applications. *ACS Nano* **2020**, *14* (10), 13047−13055.

(41) Hui, L.; Chen, C.; Kim, M. A.; Liu, H. Fabrication of DNA-Templated Pt Nanostructures by Area-Selective Atomic Layer Deposition. *ACS Appl. Mater. Interfaces* **2022**, *14* (14), 16538−16545.

(42) Michelson, A.; Subramanian, A.; Kisslinger, K.; Tiwale, N.; Xiang, S.; Shen, E.; Kahn, J. S.; Nykypanchuk, D.; Yan, H.; Nam, C.-

Y.; Gang, O. Three-Dimensional Nanoscale Metal, Metal Oxide, and Semiconductor Frameworks through DNA-Programmable Assembly and Templating. *Sci. Adv.* **2024**, *10* (2), No. eadl0604.

(43) Ober, M. F.; Baptist, A.; Wassermann, L.; Heuer-Jungemann, A.; Nickel, B. In Situ Small-Angle X-Ray Scattering Reveals Strong Condensation of DNA Origami during Silicification. *Nat. Commun.* **2022**, *13* (1), No. 5668.

(44) Wang, Y.; Dai, L.; Ding, Z.; Ji, M.; Liu, J.; Xing, H.; Liu, X.; Ke, Y.; Fan, C.; Wang, P.; Tian, Y. DNA Origami Single Crystals with Wulff Shapes. *Nat. Commun.* **2021**, *12* (1), No. 3011.

(45) Wibowo, A.; Marsudi, M. A.; Amal, M. I.; Ananda, M. B.; Stephanie, R.; Ardy, H.; Diguna, L. J. ZnO Nanostructured Materials for Emerging Solar Cell Applications. *RSC Adv.* **2020**, *10* (70), 42838−42859.

(46) Zhao, Y.; Sarhan, R. M.; Eljarrat, A.; Kochovski, Z.; Koch, C.; Schmidt, B.; Koopman, W.; Lu, Y. Surface-Functionalized Au−Pd Nanorods with Enhanced Photothermal Conversion and Catalytic Performance. *ACS Appl. Mater. Interfaces* **2022**, *14* (15), 17259−17272.

(47) Stone, H. W. Solubility of Water in Liquid Carbon Dioxide. *Ind. Eng. Chem.* **1943**, *35* (12), 1284−1286.

(48) Sabirzyanov, A. N.; Il'in, A. P.; Akhunov, A. R.; Gumerov, F. M. Solubility of Water in Supercritical Carbon Dioxide. *High Temp.* **2002**, *40* (2), 203−206.

(49) Johnson, R. W.; Hultqvist, A.; Bent, S. F. A Brief Review of Atomic Layer Deposition: From Fundamentals to Applications. *Mater. Today* **2014**, *17* (5), 236−246.

(50) Qi, J.; Zhang, W.; Cao, R. Porous Materials as Highly Efficient Electrocatalysts for the Oxygen Evolution Reaction. *ChemCatChem* **2018**, *10* (6), 1206−1220.

(51) Bathla, A.; Lee, J.; Younis, S. A.; Kim, K.-H. Recent Advances in Photocatalytic Reduction of CO2 by TiO2− and MOF−Based Nanocomposites Impregnated with Metal Nanoparticles. *Mater. Today Chem.* **2022**, *24*, No. 100870.

(52) Chen, Z.; Duan, X.; Wei, W.; Wang, S.; Ni, B.-J. Iridium-Based Nanomaterials for Electrochemical Water Splitting. *Nano Energy* **2020**, *78*, No. 105270.

(53) Abbott, D. F.; Lebedev, D.; Waltar, K.; Povia, M.; Nachtegaal, M.; Fabbri, E.; Copéret, C.; Schmidt, T. J. Iridium Oxide for the Oxygen Evolution Reaction: Correlation between Particle Size, Morphology, and the Surface Hydroxo Layer from Operando XAS. *Chem. Mater.* **2016**, *28* (18), 6591−6604.

(54) Kim, Y. J.; Lim, A.; Kim, J. M.; Lim, D.; Chae, K. H.; Cho, E. N.; Han, H. J.; Jeon, K. U.; Kim, M.; Lee, G. H.; Lee, G. R.; Ahn, H. S.; Park, H. S.; Kim, H.; Kim, J. Y.; Jung, Y. S. Highly Efficient Oxygen Evolution Reaction via Facile Bubble Transport Realized by Three-Dimensionally Stack-Printed Catalysts. *Nat. Commun.* **2020**, *11* (1), No. 4921.

(55) Bernt, M.; Schramm, C.; Schröter, J.; Gebauer, C.; Byrknes, J.; Eickes, C.; Gasteiger, H. A. Effect of the IrOx Conductivity on the Anode Electrode/Porous Transport Layer Interfacial Resistance in PEM Water Electrolyzers. *J. Electrochem. Soc.* **2021**, *168* (8), No. 084513.

(56) Alia, S. M.; Reeves, K. S.; Cullen, D. A.; Yu, H.; Kropf, A. J.; Kariuki, N.; Park, J. H.; Myers, D. J. Simulated Start-Stop and the Impact of Catalyst Layer Redox on Degradation and Performance Loss in Low-Temperature Electrolysis. *J. Electrochem. Soc.* **2024**, *171* (4), No. 044503.

(57) Cherevko, S.; Geiger, S.; Kasian, O.; Kulyk, N.; Grote, J.-P.; Savan, A.; Shrestha, B. R.; Merzlikin, S.; Breitbach, B.; Ludwig, A.; Mayrhofer, K. J. J. Oxygen and Hydrogen Evolution Reactions on Ru, RuO2, Ir, and IrO2 Thin Film Electrodes in Acidic and Alkaline Electrolytes: A Comparative Study on Activity and Stability. *Catal. Today* **2016**, *262*, 170−180.